Solid Freeform Fabrication 2019: Proceedings of the 30th Annual International
Solid Freeform Fabrication Symposium – An Additive Manufacturing Conference
Reviewed Paper

INTEGRATED HARDFACING OF STELLITE-6 USING HYBRID MANUFACTURING PROCESS

M. Praniewicz[*], T. Feldhausen[*†], S. Kersten[*], J. Berez[*], E. Jost[*], T. Kurfess[†], C. Saldana[*]
[*] Georgia Institute of Technology, Atlanta, GA 30332
[†] Oak Ridge National Laboratory, Knoxville, TN 37932

Abstract

Hybrid manufacturing systems provide a platform for integrated additive, subtractive and inspection methods on a single machine setup. The present work explores use of hybrid manufacturing for hardfacing of performance components for improving wear resistance. In this work, Stellite-6 was applied to a 410 stainless steel substrate using a hybrid manufacturing system incorporating multi-axis directed energy deposition and machining. Experimental testing was conducted to determine the effects of hybrid manufacturing parameters on internal porosity, surface porosity and microstructure in the cladded material, as well as on the roughness of the final machined surface. Correlation between porosity measurements made by x-ray tomography and surface inspection is presented and determination of ideal process parameters for hardfacing of components using hybrid manufacturing systems is briefly discussed. A deposition process is presented and implemented on a large industrial component. The component is inspected using dye-penetrant testing and metallographic techniques.

Introduction

A product's lifecycle is often limited, not due to fracture, but rather to wear over time. Eventually, worn parts lose dimensional accuracy and functionality. In order to extend a component's lifecycle, one solution is to improve wear resistance or repair parts once they have worn down to an unusable state. Currently, there are different processes available to improve the wear resistance of steel parts including: heat treatment, surface alloying, and application of a more wear resistant material to the surface [1]. Hardfacing refers to the latter process whereby a harder or wear-resistant material is applied to a base metal by welding [2]. Hardfacing can be performed as a value-added process on a new part or as a repair process thereby increasing the functional life of the component. This process is widely used in a variety of industries including mining, steel manufacturing, sugar refinery, petrochemical, farming, and others [3].

In hardfacing, material is added to the surface through a process of welding or joining. Many different welding processes can be used to deposit metal onto the parent surface. However, many of these processes suffer from high thermal input leading to higher dilution rates and larger heat affected zones (HAZ) [4]. Dilution is defined as the ratio of area of the substrate melted divided by the total area of the weld. Increased temperatures can also result in distortion of the parent geometry. Consequently, directed energy deposition (DED) is a desirable technique because it is highly accurate and repeatable and involves lower and more focused heat input [5]. Compared with other thermo-mechanical processes, laser-cladding / DED is capable of generating coatings with lower dilution levels and a more refined microstructure [6]. In DED, feedstock, in wire or powder form, is fed into a melt pool generated by a high-power laser. In the coaxial laser cladding process, the powder absorbs some of the laser energy and becomes partially melted before impacting the base material. The remaining, unattenuated laser energy is absorbed into the surface

of the substrate generating a melt pool, which allows for the formation of strong metallurgical bonding between the two materials [7]. As the laser scans the surface of the part material is built up in its path. If adjacent tracks overlap to a sufficient degree and the cladded tracks have satisfactory geometric characteristics then fully dense, porosity free layers can be built. Multiple layers can be deposited in the same region to build geometric features or thick coatings. In the blown powder configuration, an inert carrier gas, such as argon, is used to deliver the feedstock to the melt pool while the entire process is shrouded in an inert shielding gas to prevent oxidation. Similar to many AM processes, post processing is required on DED components to meet geometric accuracy or surface quality specifications. Post processing techniques include, but are not limited to, machining, electrical discharge machining (EDM), or surface treatments such as sandblasting or shot peening.

Cobalt-based alloys are a popular and widely used hardfacing material due to their excellent hardness, resistance to corrosion, and ability to retain mechanical properties at elevated temperatures. Stellite alloys are popular, trade named Co-alloys, of which Stellite-6 is the most common. Stellite-6 has proven to have a balanced mix of desirable mechanical properties, as compared with other available Co-alloys. Stellite-6 combines high strength and ductility with outstanding wear resistance while maintaining high hardness at elevated temperatures; showing good resistance to oxidation at elevated temperatures, which is necessary for various pressure vessel applications [8, 9]. The favorable hardness and wear properties of Stellite-6 are derived from carbides that form in the alloy and are suspended within the cobalt matrix. These carbides are primarily chromium-carbide M_7C_3 groups which make up approximately 16-17% of the alloy by volume (other carbide groupings are also present in lower quantities) [10, 11]. Because of low heat input associated with rapid cooling of the laser cladding process, the resulting microstructure of the clad layer is much finer than with other processes such as Plasma Transferred Arc Welding [9]. It has been reported that the hardness of Stellite 6 coatings is strongly dependent on solidification microstructures, with a refined microstructure generally being favorable [6]. It is worth considering the safety hazards using this powdered alloy, particularly the powder toxicity. Stellite-6, and the majority of other cobalt-based alloys, have a high oral toxicity compared to nickel or iron based hardfacing alloys [12]. However Cobalt family of hard facing alloys provides an unsurpassed combination of wear resistance, corrosion resistance, and usability in high temperature applications [11].

Hybrid manufacturing seeks to reduce potential setup and material handling errors associated with disjointed manufacturing processes by combining them within one machine. Of note are hybrid systems which combine additive manufacturing with machining. While hybrid manufacturing systems have been a subject of research for some time [13, 14], commercial systems have only been recently introduced [15, 16]. These systems can be used to refurbish or create new components with up to a 50% reduction in manufacturing costs [17]. Industrial implementation has already occurred in the mold and die repair industry [18], and has opened the door to further industrial application development [19-21]. For creation of most components, additive manufacturing (AM) is often a cost prohibitive when compared to other manufacturing methods. Yet, research has shown that the implementation of hybrid manufacturing can reduce material costs up to 97% in the manufacture of complex components by selectively producing features using deposition as opposed to machining from a single billet [15].

Significant savings could be realized by replacing traditionally separate hardfacing and machining operations with a hybrid process. The low dilution of DED and accurate numerical control should improve the quality of deposition while also reducing setup time between processes. The development and analyses of this process is demonstrated via the framework of a specific application – a component which calls for hardfacing with the Stellite-6 alloy. This component is a 410 stainless steel ring of approximately 8in in outer diameter and 5in in inner diameter. Hardfacing is applied to a portion of the face and inner chamfered edge of the ring – a geometry typical of many wear-heavy applications. First, initial tests were performed on test geometries to determine proper parameters for the process. Section two discusses the materials and methodology used the experiments. Section three presents the results observed in the sample studies and the on-component execution. Section four contains an additional discussion on the results observed and present additional findings to give better insight into the on-component execution. Section five summarizes the main conclusions drawn from this study and proposes the future course of study.

Methodology

The system used in this project was a commercially available hybrid manufacturing machine, Mazak VC500-AM, which combines a high-speed milling spindle with a coaxial 1-kilowatt 1 mm spot-size diameter continuous wave Ytterbium fiber laser blown powder (coaxial) DED system in a multi-axis machine tool. The elemental composition of the Stellite 6 powder used in this study, as reported by the powder manufacturer [22], is reported Table 1.

Table 1: Stellite-6 Chemistry

Elem.	Co	Cr	W	Fe	Si	Ni	C	Mo	Mn
%	Bal.	30.3	5.0	1.9	1.5	1.20	1.12	0.6	0.04

To quantify the morphology of the powder used in this study, a scanning electron microscope (SEM) equipped with a Schottky FEG gun operating at an acceleration voltage of 15 kV was employed. Figure 1a shows satellites attached to the powder as is typical in atomized metal powders. Using a custom MATLAB algorithm for segmentation and powder size characterization, the size distribution of powder seen in Figure 1b was obtained. Particle diameter was calculated by calculating a diameter based on the area of each powder particle measured.

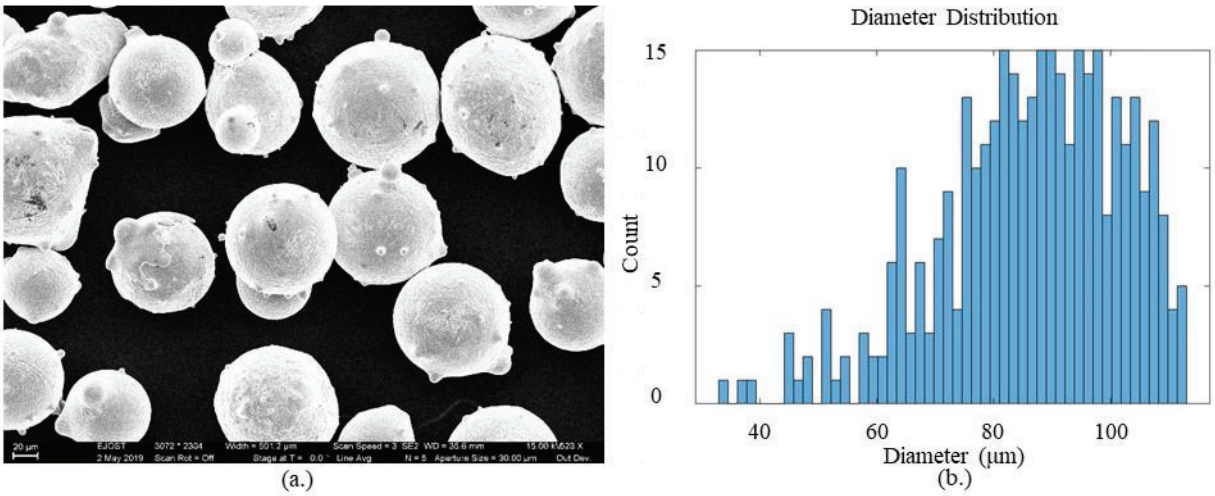

Figure 1: SEM Powder Characterization. a) SEM image of powder at ~500x magnification. b) Powder size distribution

After characterization of powder was complete, an initial investigation of deposition parameters could begin. Small test cubes which could be machined to 8mm per side were created to characterize subsurface porosity while mimicking the deposition of bulk material. Traversal speed (100mm/min – 300mm/min) and laser powder (400-600W) were varied across the tests. Held constant in these tests were the carrier gas flowrate (5 L/min), the shielding gas flowrate (10 L/min), the nozzle gas flowrate (2 L/min), powder feed disk speed (70%), and toolpath geometry. These tests were evaluated for build quality, and overall build height. The specific settings used in the tests and the layout on the build geometry can be seen in Table 2. The tool path geometry utilized was a raster pattern whose orientation was alternated by 90 degrees from layer to layer, as seen in Figure 2.

Table 2: Initial characterization sample parameters

Sample	Speed (mm/min)	Power (W)	Layer Height (mm)	Number of Layers
1	200	400	0.53	16
2	200	600	0.53	16
3	300	600	0.53	16
4	300	400	0.53	16
5	100	400	0.53	16
6	200	400	0.5	17

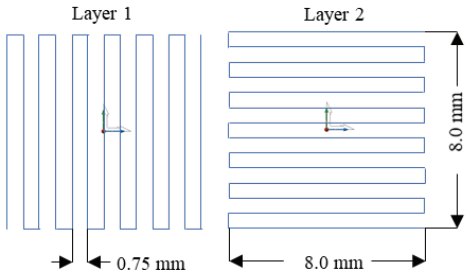

Figure 2: Tool path geometry for initial testing

Based on observations that will be presented in the results section, a second round of tests were performed with the selected parameters which focused on tuning the toolpath geometry. The goal of the second set of tests was to produce samples with little porosity and as-designed build height. In these samples, laser power was held constant at 400W. The powder delivery and gas flow rates were held constant at the previously stated values. The laser scanning speed, layer height, number of layers, and toolpath type were manipulated while analyzing the build geometry and surface porosity after machining. In AM components, a contour path is often used to surround an internal raster pattern to improve external surface quality, and better simulates conditions that will be used in the deposition strategy of the actual component. The different tool path types can be seen in Figure 3.

The contour tool path was executed for three of the samples to examine the effect of toolpath type on the component geometry and the surface porosity (post-machining). The laser scanning speed and layer height were manipulated to investigate the effect of minor feed rate changes on the overall build height. The parameters used for each sample can be seen in Table 3.

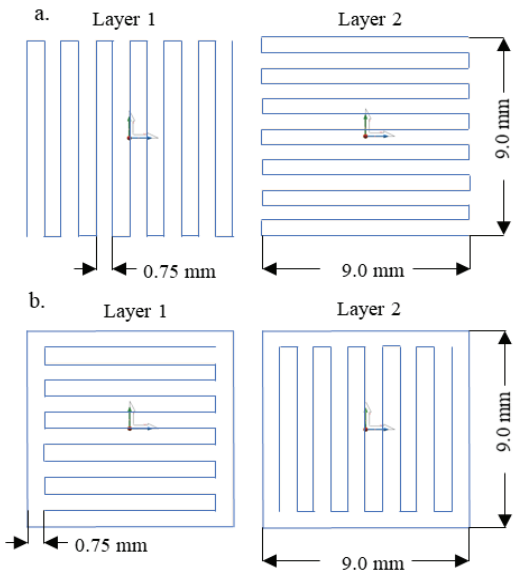

Figure 3: Toolpath geometry a) Raster b) Raster with exterior contour

Table 3: Parameters used for secondary testing

Sample	Speed (mm/min)	Layer Height (mm)	Number of Layers	Toolpath Type
7	200	0.53	19	Raster
8	200	0.5	20	Raster
9	200	0.53	19	Raster w/ Contour
10	200	0.5	20	Raster w/ Contour
11	238	0.5	20	Raster w/ Contour
12	238	0.5	19	Raster

After deposition in this test was completed, the samples were machined to size on five sides for subsurface inspection. This was done using a 9.525 mm diameter four flute end mill at a surface speed of 30.48 m/min and a feed-rate of 0.03 mm/tooth. After the machining was complete, the samples were separated from the substrate using wire electrical discharge machining (EDM). The samples were then qualified using non-destructive techniques.

X-ray computed tomography (CT) was utilized to nondestructively inspect the separated samples. Using a VisiConsult XRH222 CT machine, samples were inspected at an acceleration voltage of 220 kV and 3.6 mA. A prefilter of 1 mm Cu was used to mitigate beam hardening effects common in laboratory CT sources. The traditional Feldkamp reconstruction algorithm was used to reconstruct 700 radiographic projections into a 3D volume of each inspected coupon at a resolution of 65 µm/voxel. The five machined surfaces of the samples were inspected for defects which surpassed the maximum allowable defect diameter of 381 µm using a Leica DVM6 10-megapixel digital microscope.

After all samples were evaluated and processing parameters were chosen, deposition was completed on the component. The parameters used in sample nine were utilized to deposit on the actual component. The toolpath for this process was completed in two distinct sections, as seen in Figure 4. The chamfered section at 45 degrees was completed first at a fixed orientation of the machine's B axis while the C axis rotated 360 degrees. After one path was completed, the C axis was incremented by 30 degrees in order to stagger the start position of each concentric ring around

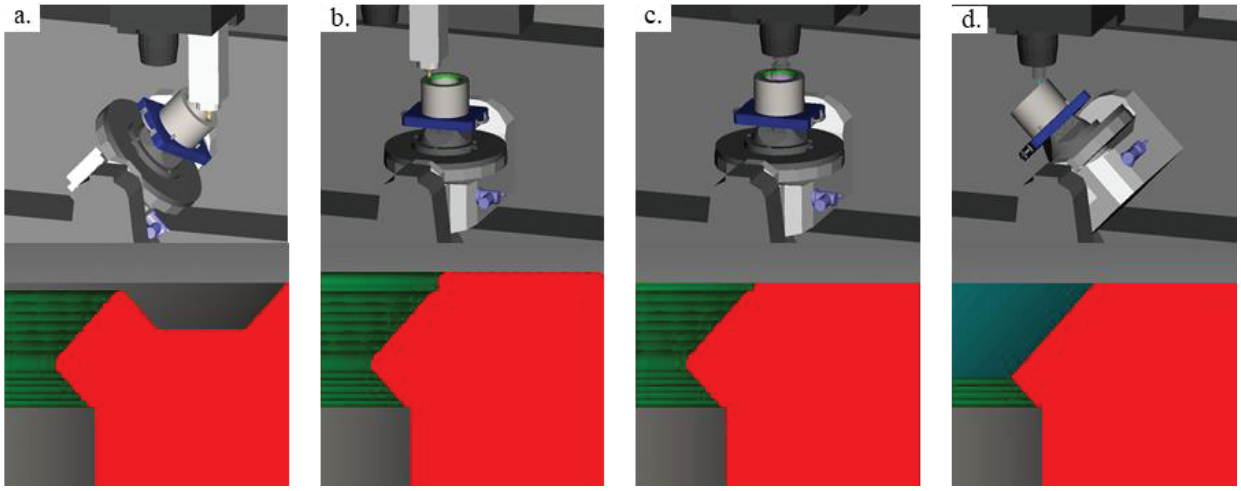

Figure 4: Machine simulation (top) and simulation of resultant geometry (below) after each step. The cross sectioned face is shown it red with deposited geometries shown in green. a) Chamfer deposition b) Vertical deposition c) Face milling d) Swarf milling

the component's axis. Once the chamfered region had been completed, the B axis was repositioned to 0 degrees, and concentric rings were once again deposited using an incremental rotation of 30 degrees between each stepover. This portion of the deposition did not utilize the rotation of the C axis and instead utilized the movement of the X and Y axes. After deposition, the component was allowed to cool to room temperature. The top face of the cylindrical component was milled using a facing strategy, followed by a swarf machining strategy to bring the chamfer to final form. Both of these milling strategies utilized identical processing conditions to those previously stated.

The application for which this process was developed calls for fluorescent dye penetrant inspection as a pass/fail measure to asses surface porosity with no pores over 381 µm allowable in the final as-machined surface. This inspection method (more often referred to as 'dye-pen') is commonly utilized in industry to inspect parts for surface porosity and cracks in as-manufactured castings, forgings, welded components, machined components, and structurally tested components. ASTM standard E1417 [23] defines penetrant types, inspection methods, equipment and personnel requirements, and best practices. The penetrant used in this application is a product of Magnaflux, ZYGLO ZL-60D, which is utilized in combination with the developer ZYGLO ZP-

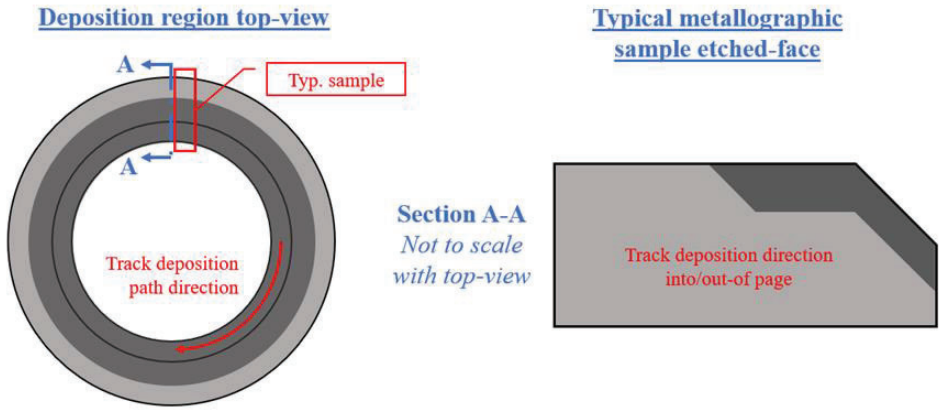

Figure 5: A schematic representing the area of the deposition from which metallographic samples, with the 410 substrate shown lighter than the Stellite-6, were taken from, and the face which was polished an etched for microscopy.

9F (both commercially available). This is a fluorescent penetrant which has high visibility when exposed to UV light and is designed for *level 2* sensitivity for test *type 1*, *method A* or *C* as defined by ASTM E1417. As a *level 2* penetrant, it has 'medium sensitivity' and is adequate for identifying the maximum allowable flaw size for this application while not providing too many false positives. Per E1417, inspection is to be performed by-eye by an ANSI/ANST certified inspector, which was not possible for this study.

The process of inspection defined by E1417 *method C* was utilized. The deposition region, previously finish-machined and sectioned from the bulk part using wire EDM, was cleaned with isopropyl alcohol, removing all oils, grease, and surface contamination that could affect penetrant effectiveness. After drying, aerosolized penetrant was applied and left to dwell for 10-30 min after which excess penetrant was removed via light wiping of the part with a first a dry then a damp, clean, lint-free cloth. After completely drying the aerosolized developer is applied and left to dwell for 10-60 min. Then, as with the penetrant, excess developer is removed. The deposition region was then inspected with a UV lamp, corresponding to the requirements of the E1417. If no fluorescent traces were identified a part 'passed' inspection. If traces were identified they were assessed as a false or true positive by the inspector and accordingly passed or failed. In this study photography was performed in a darkened environment primarily illuminated by UV light to record results. A Nikon D200 DSLR camera was used with a 105 mm focal length, f/2.8 maximum aperture, 35 mm format lens. With a 1:1 reproduction ratio, photos closely mimic the resolving ability of the human eye under close inspection of the part, the method of inspection that this test is designed for.

Samples were taken from the component for additional metallographic analysis to asses deposit-substrate fusion, deposit dilution, deposit microstructure, and porosity. A representation of the sectioned geometry can be seen in Figure 5. This produced a face transverse to the deposited tracks for subsequent polishing and etching, also pictured in Figure 5. Once sectioned, samples were mechanically polished with silicon carbide abrasive paper from 240 to 4000 grit, suspended diamond of 9 to 1 um in size, and finally vibratory polished with .05 um alumina. Etching was performed with aqua regia with samples fully immersed in the agitated etchant for approximately 45 seconds. Samples were then cleaned and inspected via digital microscopy with a Leica DVM6 microscope.

Results

Parameter Test Results

Figure 6 shows the samples created during the initial parameter testing phase. Samples two and three yielded nozzle sputtering and overall poor deposition, and the process was terminated prematurely after the fourth layer. Sample five was also terminated after the sixth build layer after it was observed that clearance between the nozzle and the deposited material had significantly decreased. Sample four was built to completion. However, the layer height for this condition was less than initially anticipated. This caused the deposition zone to move out of the focal plane of the laser and yielded a component far shorter than the intended height. Samples one and six yielded geometry close to the intended design and the processing parameters used here were selected for further testing.

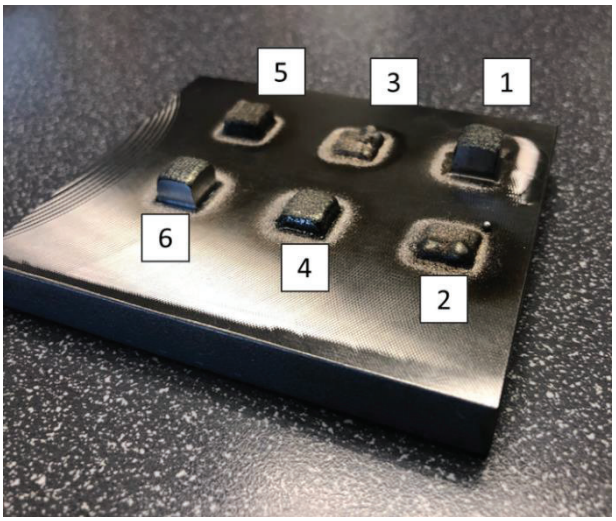

Figure 6: Results of initial parameter testing

Secondary testing showed encouraging results. Comparing the effect of the tool path type, it was seen that the use of an exterior contour path improved the form of the top surface of the deposition. Between samples seven and nine, a more consistent (flat) surface was observed as a result of the contour toolpath used in sample nine. This can be observed in Figure 7a. Sample ten, which utilized a contour pass, again showed better form on the top surface of the sample compared to that of sample eight. However, significant overbuild was observed for these samples. This can be seen in sample ten in Figure 7b., in which the machining process has been interrupted to reveal the depth of cut taken to produce the final top surface. A reduction in overall as-deposited height in samples eleven and twelve was noted where the traversal speed was increased. The samples were then examined for internal porosity.

Following thresholding of CT data to determine the part surfaces of each sample, a porosity identification algorithm internal to Volume Graphics VGSTUDIO MAX 3.2, a CT data analysis software, was used to identify internal pores. Image processing algorithms were used to suppress the interference of image artifacts such as ring artifacts in porosity identification. CT inspection results shown in Figure 8, below, revealed that no internal pores beyond the inspection criterion

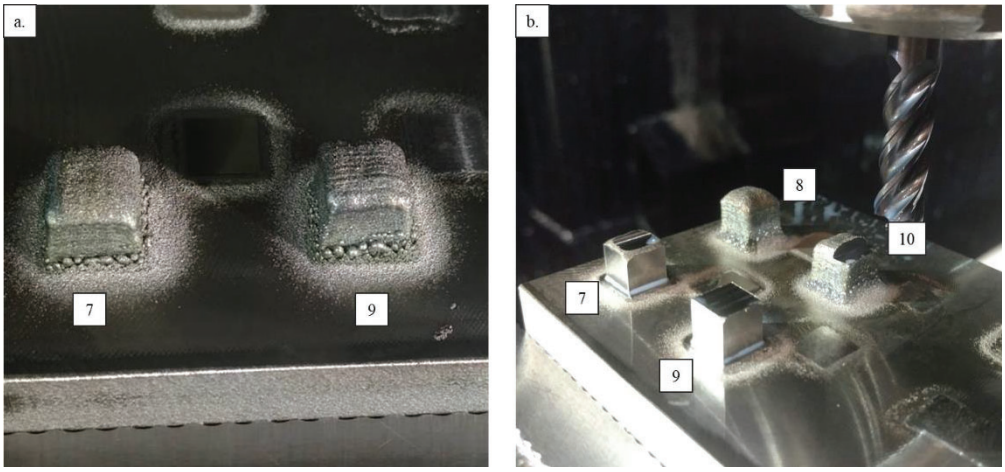

Figure 7: Creation of secondary samples a) Deposition of samples 7 and 9 b) Machining of samples 7-10

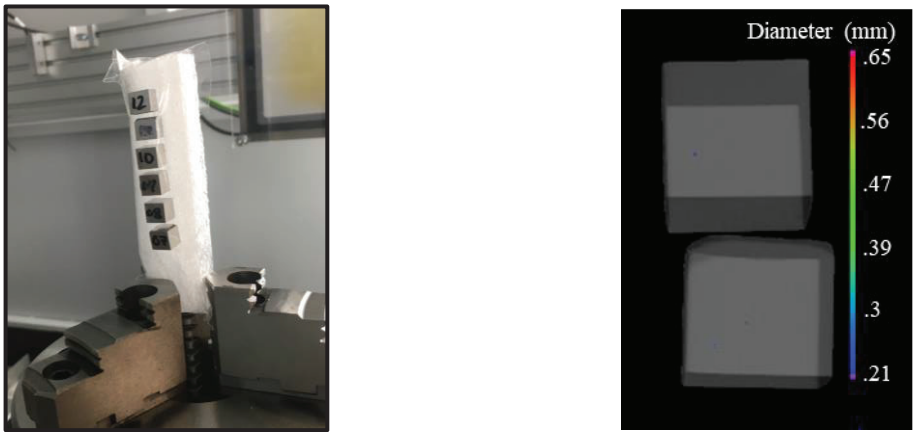

a) b)

Figure 8: CT of inspection coupons. a) Fixtured samples in CT machine. b) 85% Transparent CT analysis results of samples 11 and 12 showing no internal porosity in excess of specification.

of 381 µm diameter existed in any of the test coupons, meaning that print parameters were sufficient to build parts passing the manufacturing criterion for internal porosity.

The machined surface inspection yielded similar results. No visible surface defects were noted on samples seven through nine and eleven. Two surface pores were found on face three of sample ten. These are displayed in subsets of the overall face in Figure 9 and measured 155 µm (top) and 171 µm (bottom) in maximum diameter. A similar surface defect was also found on face five of sample twelve which measured 104 µm in maximum diameter. While surface defects were observed in these samples, they were small enough to still meet the inspection criteria. However,

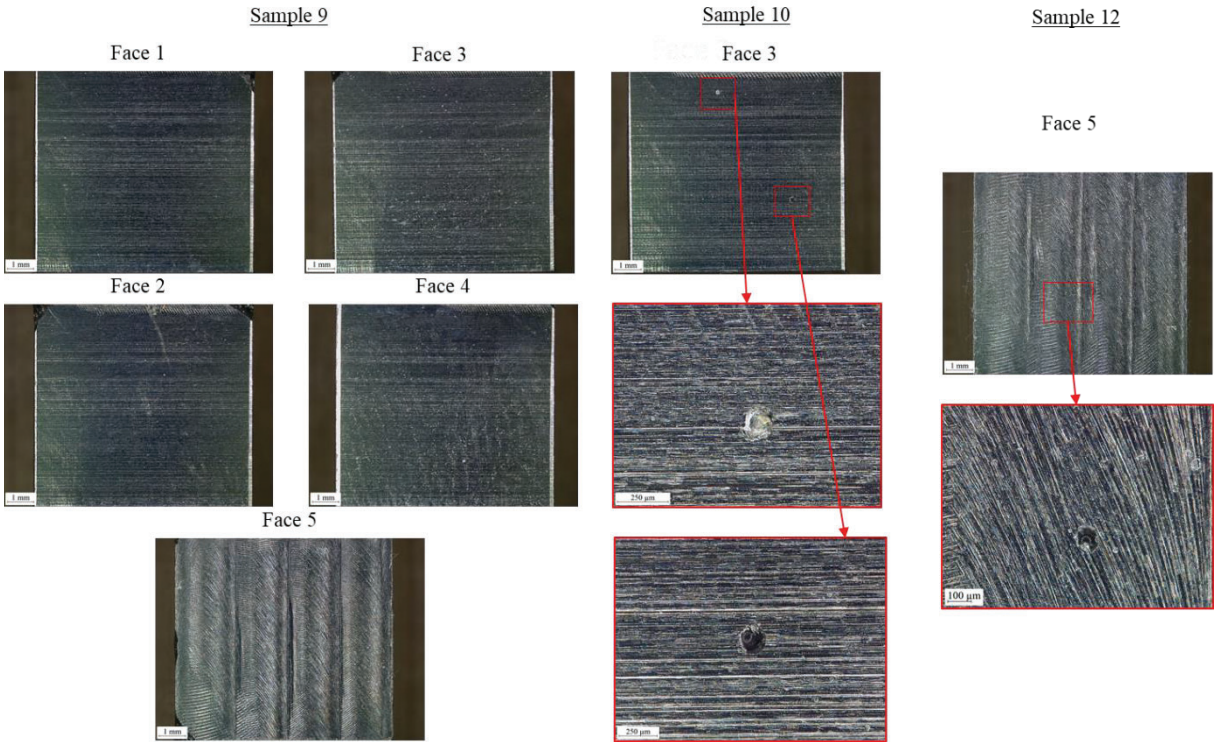

Figure 9: Digital microscopy images of several samples 9,10,12

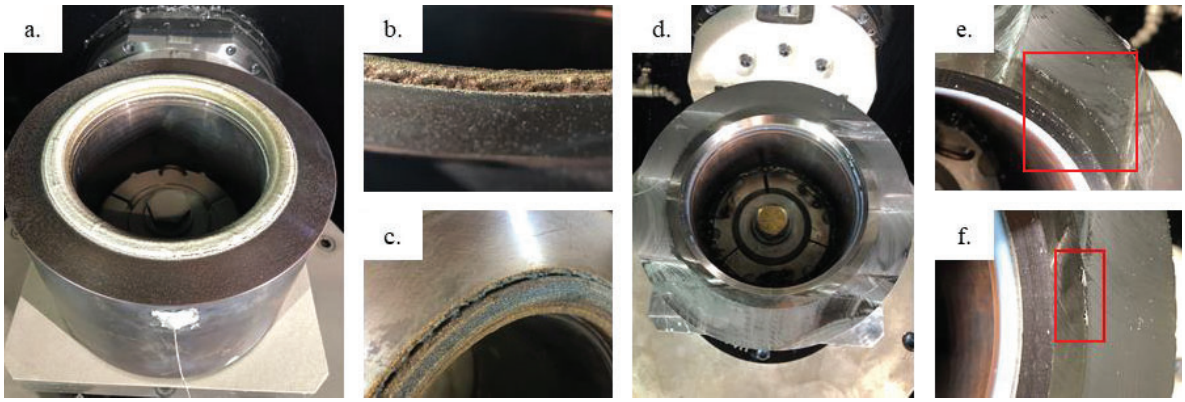

Figure 10: Images of the completed process. The overall component is shown after the deposition a) and defects noted from the deposition process b) & c). The as-machined component d) is shown along with observed defects in one section of the component e) & f).

with these small defects in mind, the parameter set from sample nine was chosen for the on-component implementation.

On-component results

The completed component can be seen in Figure 10. Subset (a.) of this figure shows the component following the deposition process. One region of the component appears to have insufficient coverage of the substrate. This can be seen in Figure 10c. However, the opposite quadrant of the component appears to have an excessive buildup of material, shown in Figure 10b. Figure 10d. shows the component after the completed machining process. Overall, the component shows good machinability and adequate surface finish for the process. However, surface defects are still present and can be seen in Figure 10 e. and f. These surface defects are more apparent in the dye penetrant inspection.

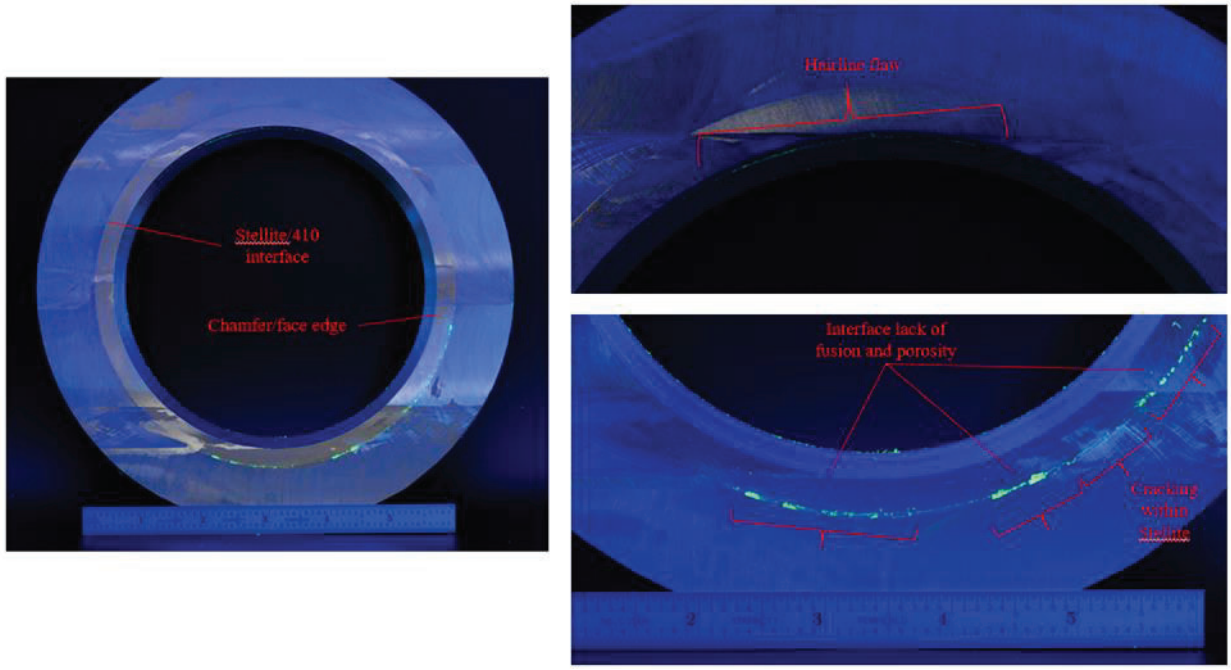

Figure 11: Photos of fluorescent dye-pen test results under UV light. Note that the fluorescent traces on the inner diameter of the specimen are not indications of flaws, but simply remnants of the penetrant adhering to the sharp edge on that area of the specimen.

Figure 11 displays a selection of photos from the deposition region. The specimen clearly displays many strung-together large pores on the Stellite-410 interface on the bottom right and left quadrants of the article. A thin and semi-continuous hairline pore on the chamfered section of the Stellite deposit is also visible on various sections, most clearly seen in the topmost portion of the article. These findings correspond with pores and cracks seen in the sectioning of test articles for metallography, as later discussed. This clearly fails the dye-pen test, with multiple pores of an unacceptable size in varying locations. The authors believe that these regional defects are the result of asymmetric gas flow from the deposition, as minor damage to the nozzle gas outlet was discovered after testing.

Discussion

Figure 12 displays a sample from the top portion of the machined component, sectioned, polished, and etched according to earlier descriptions, similar to the section view in Figure 5. The inset of 12a from Ref. [24] displays a classic welding solidification microstructure as seen in cross-section view of the weld bead, with a section-line drawn indicating the sectioning orientation of this sample.

Several aspects are of note in these micrographs. As can be seen clearly, the crack seen on the surface of the chamfered section (observable by eye and in dye-pen testing) of the machined test article continues down to the Stellite-substrate interface. This indicates that lack of fusion during the deposition of the first layer, potentially aggravated by residual stresses, could have contributed to the crack in this portion of the test article. Also of note is the extremely low dilution of the Stellite-6 track, approximately 7%. This low dilution level is somewhat typical of laser

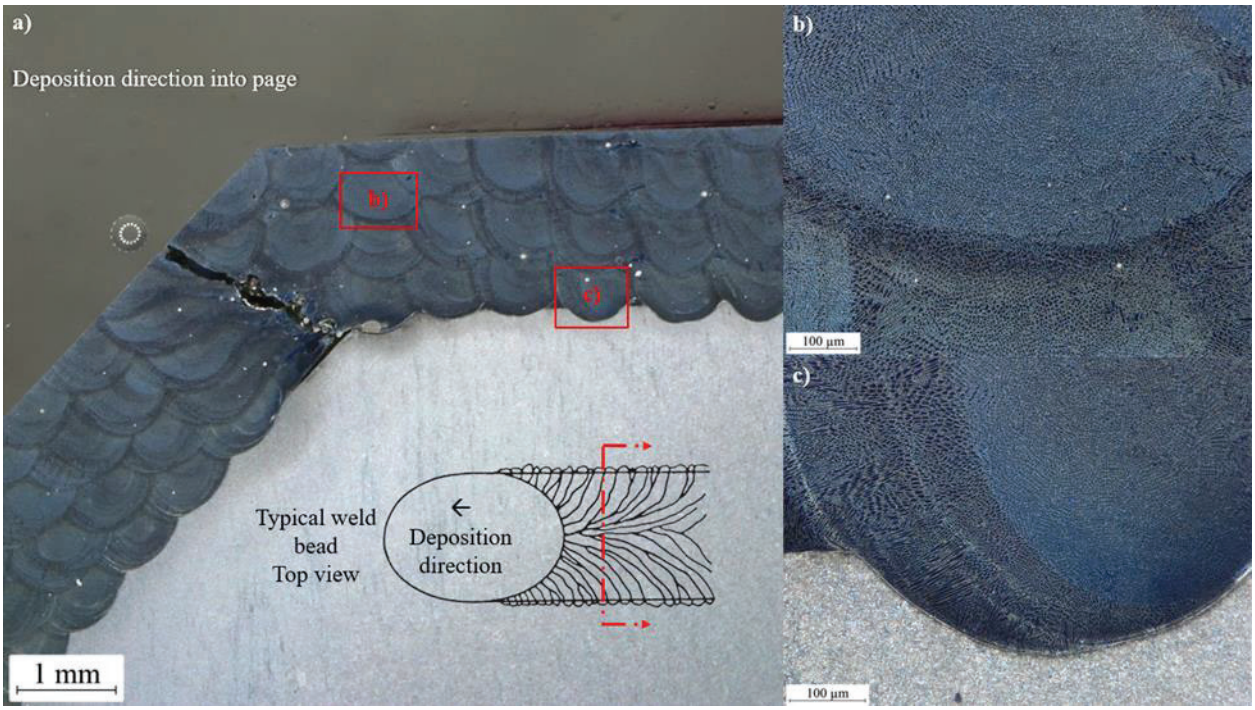

Figure 12: a) Micrograph of a sample from the bulk material sectioned transverse to the direction of deposition. The sectioning lines correspond to the presented faces of the displayed micrographs. b) A track in the third deposition layer showing extremely rapid refinement of microstructure. c) A track from the first layer of deposition, showing a clear evolution of microstructure.

cladding / DED methods (depending on the deposition parameters used) [25-27], and indicates success from an efficiency-of-deposition standpoint in this application.

The solidification microstructure of Stellite-6 via laser cladding and other high-energy density deposition methods has been studied previously, and is consistently composed of a fine cellular and dendritic microstructure which is displayed in this application as well [25-27]. This refinement is due to the extremely high thermal gradients and solidification rates that laser cladding produces [26]. The refined microstructure increases the hardness of the deposit, and it is reasoned that it also improves wear resistance properties, due to the more evenly distributed interdendritic carbides, though wear testing would be needed to confirm this hypothesis for this application [27].

Poor dilution at the interface of the chamfered and flat section implies a degradation of the deposition condition in this region, which points to poor process design as the cause of failure. Furthermore, significant melt pool deformation, specifically degradation in the geometry of the bead, can be seen at this interface as a result of using a deposition strategy using two discrete build phases. A deposition strategy which smoothly transitions between the chamfered and flat regions within each layer will be investigated to resolve this. Along with continuing work on the blown powder system, parallel development of hot-wire hybrid technologies are being pursued by the team. The hot-wire system can achieve much higher deposition rates due to a more powerful laser, larger spot diameter, and more efficient material utilization, this potentially providing conditions necessary for defect-free fabrication.

Conclusion

In this work, an exploration of implementing a hard-facing process which involved the deposition of Stellite-6 onto a 410 stainless steel substrate within a commercial hybrid manufacturing system was conducted. Initial test samples were created to characterize process parameters. Further samples investigated the effect of process parameters on build quality, internal porosity, and surface defects revealed by machining. Finally, the selected process parameters were used in the on-machine implementation. All samples produced within the second round of tests were shown to comply with the specified inspection criteria. However, the process caused flaws within the part, including surface voids and internal cracking. Future work will focus on modifications to the process design and additional microstructure characterization.

Acknowledgements

The authors work like to acknowledge Mazak Corporation for their support of this project and the consignment of the Mazak VC500-AM used in this study, and specifically to Mike Finn for his assistance in this project. The authors would also like to acknowledge Omar Elsayed, who participated in the metallography work presented here. The authors would like to acknowledge partial support from the National Physical Sciences Consortium (NPSC) for fellowship support for M. Praniewicz.

References

[1] H. Kashani, A. Amadeh, and M. Farhani, "Improvement of wear resistance of hot working tool steel by hardfacing Part 1–Effect of microstructure and hardness," *Materials science and technology,* vol. 23, no. 2, pp. 165-170, 2007.

[2] B. Khanpara and P. Rathod, "A Review On Hard Surface Coatings Applied Using Stellite Hardfacing Techniques," *International Journal of Engineering Technology, Management and Applied Sciences,* vol. 5, no. 4, 2017.

[3] (2019, 6/25/2019). *Hardfacing: Oerlikon solutions for hardfacing applications*. Available: https://www.oerlikon-welding.com/applications/solutions-hardfacing-applications

[4] A. Frenk, M. Vandyoussefi, J. D. Wagniere, A. Zryd, and W. Kurz, "Analysis of the laser-cladding process for stellite on steel," (in English), *Metallurgical and Materials Transactions B-Process Metallurgy and Materials Processing Science,* vol. 28, no. 3, pp. 501-508, Jun 1997.

[5] E. Diaz, J. M. Amado, J. Montero, M. J. Tobar, and A. Yanez, "Comparative study of Co-based alloys in repairing low Cr-Mo steel components by laser cladding," (in English), *Laser Assisted Net Shape Engineering 7 (Lane 2012),* vol. 39, pp. 368-375, 2012.

[6] N. Hutasoit, W. Y. Yan, R. Cottam, M. Brandt, and A. Blicblau, "Evaluation of Microstructure and Mechanical Properties at the Interface Region of Laser-Clad Stellite 6 on Steel Using Nanoindentation," (in English), *Metallography Microstructure and Analysis,* vol. 2, no. 5, pp. 328-336, Oct 2013.

[7] A. Kusmoko, D. Dunne, and H. J. Li, "Effect of Heat Input on Stellite 6 Coatings on a Medium Carbon Steel Substrate by Laser Cladding," (in English), *Materials Today-Proceedings,* vol. 2, no. 4-5, pp. 1747-1754, 2015.

[8] F. Luo, A. Cockburn, R. Lupoi, M. Sparkes, and W. O'Neill, "Performance comparison of Stellite 6® deposited on steel using supersonic laser deposition and laser cladding," *Surface and Coatings Technology,* vol. 212, pp. 119-127, 2012.

[9] M. M. Ferozhkhan, M. Duraiselvam, K. G. Kumar, and R. Ravibharath, "Plasma Transferred Arc Welding of Stellite 6 Alloy on Stainless Steel for Wear Resistance," (in English), *1st Global Colloquium on Recent Advancements and Effectual Researches in Engineering, Science and Technology - Raerest 2016,* vol. 25, pp. 1305-1311, 2016.

[10] U. O. B. de Oliveira, *Laser treatment of alloys: processing, microstructure and structural properties*. 2007.

[11] B. Hu, "Metal and Alloy Powders for Welding, Hardfacing, Brazing, and Soldering," in *ASM Handbook, Volume 7, Powder Metallurgy*, P. Samal and J. Newkirk, Eds.: ASM International, 2015, pp. 770-782.

[12] "JK7112/JK112/Stelcar 9672 Powder," in "Stellite - Welding powder," Kennametal Inc, 1600 Technology Way Latrobe, PA 15650, USA2014-09-08 2014, Available: http://exocor.com/downloads/msds/SCMS1-Stelcar%209672%20JK112%20Powder-0917.pdf.

[13] J. B. Jones, P. McNutt, R. Tosi, C. Perry, and D. I. Wimpenny, "Remanufacture of turbine blades by laser cladding, machining and in-process scanning in a single machine," in *23rd Annual International Solid Freeform Fabrication Symposium*, 2012, pp. pp.821–827, Austin, TX, USA, 2012.

[14] D.-S. Choi *et al.*, "Development of a direct metal freeform fabrication technique using CO2 laser welding and milling technology," *Journal of Materials Processing Technology,* vol. 113, no. 1-3, pp. 273-279, 2001.

[15] T. Yamazaki, "Development of a hybrid multi-tasking machine tool: integration of additive manufacturing technology with CNC machining," *Procedia CIRP,* vol. 42, pp. 81-86, 2016.

[16] A. Hansel *et al.*, "Study on consistently optimum deposition conditions of typical metal material using additive/subtractive hybrid machine tool," (in English), *7th Hpc 2016 - Cirp Conference on High Performance Cutting,* vol. 46, pp. 579-582, 2016.

[17] W. E. Frazier, "Metal Additive Manufacturing: A Review," (in English), *Journal of Materials Engineering and Performance,* vol. 23, no. 6, pp. 1917-1928, Jun 2014.
[18] L. Ren, A. P. Padathu, J. Ruan, T. Sparks, and F. W. Liou, "Three dimensional die repair using a hybrid manufacturing system," in *SFF Symposium*, Austin, TX, 2008.
[19] M. Soshi, J. Ring, C. Young, Y. Oda, and M. Mori, "Innovative grid molding and cooling using an additive and subtractive hybrid CNC machine tool," (in English), *Cirp Annals-Manufacturing Technology,* vol. 66, no. 1, pp. 401-404, 2017.
[20] M. Praniewicz, T. Kurfess, and C. Saldana, "An Adaptive Geometry Transformation and Repair Method for Hybrid Manufacturing," (in English), *Journal of Manufacturing Science and Engineering-Transactions of the Asme,* vol. 141, no. 1, p. 011006, Jan 2019.
[21] J. Liu, Y. Zheng, Y. Ma, A. Qureshi, and R. Ahmad, "A Topology Optimization Method for Hybrid Subtractive–Additive Remanufacturing," *International Journal of Precision Engineering and Manufacturing-Green Technology,* journal article March 08 2019.
[22] P. A. Corporation, "Certified Materials Report for PAC 6CO Rev F," 2019.
[23] *ASTM E1417/E1417M-16 Standard Practice for Liquid Penetrant Testing*, 2016.
[24] J. N. DuPont, "Fundamentals of Weld Solidification," in *Welding Fundamentals and Processes*, vol. 6A, T. Lienert, T. Siewert, S. Babu, and V. Acoff, Eds.: ASM International, 2011, p. 0.
[25] A. S. C. M. D'Oliveira, P. S. C. P. da Silva, and R. M. C. Vilar, "Microstructural features of consecutive layers of Stellite 6 deposited by laser cladding," (in English), *Surface & Coatings Technology,* vol. 153, no. 2-3, pp. 203-209, Apr 15 2002.
[26] T. Palmer and J. O. Milewski, "Laser Deposition Processes," in *ASM Handbook, Volume 6A, Welding Fundamentals and Processes*, T. Lienert, T. Siewart, S. Babu, and V. Acoff, Eds.: ASM International, 2011, pp. 587-594.
[27] S. Sun, Y. Durandet, and M. Brandt, "Parametric investigation of pulsed Nd: YAG laser cladding of," *Surface & Coatings Technology,* vol. 194, pp. 225-231, 2005.